Photoacoustics 28 (2022) 100413

Contents lists available at ScienceDirect

Photoacoustics

journal homepage: www.elsevier.com/locate/pacs

# Ultrasonic photoacoustic emitter of graphene-nanocomposites film on a flexible substrate

Daniele Vella [a,*], Aleš Mrzel [b], Aljaž Drnovšek [c], Vasyl Shvalya [d], Matija Jezeršek [a]

[a] Faculty of Mechanical Engineering, Laboratory for Laser Techniques, University of Ljubljana, Aškerčeva 6, 1000 Ljubljana, Slovenia
[b] Jožef Stefan Institute, Department of Complex Matter, Jamova 39, 1000 Ljubljana, Slovenia
[c] Jožef Stefan Institute, Department of Thin Films and Surfaces, Jamova 39, 1000 Ljubljana, Slovenia
[d] Jožef Stefan Institute, Department of Gaseous Electronic, Jamova 39, 1000 Ljubljana, Slovenia

ARTICLE INFO

*Keywords:*
Graphene-Polydimethylsiloxane composite
Photoacoustic materials
Laser ultrasonics
Photoacoustic lens
Acoustic cavitation

ABSTRACT

Photoacoustic devices generating high-amplitude and high-frequency ultrasounds are attractive candidates for medical therapies and on-chip bio-applications. Here, we report the photoacoustic response of graphene nanoflakes – Polydimethylsiloxane composite. A protocol was developed to obtain well-dispersed graphene into the polymer, without the need for surface functionalization, at different weight percentages successively spin-coated onto a Polydimethylsiloxane substrate. We found that the photoacoustic amplitude scales up with optical absorption reaching 11 MPa at ~ 228 mJ/cm$^2$ laser fluence. We observed a deviation of the pressure amplitude from the linearity increasing the laser fluence, which indicates a decrease of the Grüneisen parameter. Spatial confinement of high amplitude (> 40 MPa, laser fluence > 55 mJ/cm$^2$) and high frequency (Bw-6db ~ 21.5 MHz) ultrasound was achieved by embedding the freestanding film in an optical lens. The acoustic gain promotes the formation of cavitation microbubbles for moderate fluence in water and in tissue-mimicking material. Our results pave the way for novel photoacoustic medical devices and integrated components.

## 1. Introduction

Light-to-sound conversion has been implemented in many fields ranging from, photoacoustic (PA) spectroscopy [1–3], characterization of material defects [4], in-vivo PA imaging of biological tissues [5–7], and high-intensity ultrasound therapy [8]. The increasing demand for high amplitude and broadband ultrasound to achieve high spatial resolution, target a deep tissue region or manipulate nanoobjects in a microfluidic chip, has created new challenges and development of photoacoustic materials that can be integrated with optical components.

The miniaturization of traditional piezoelectric transducers from sub-MHz to MHz frequency regions can be a challenging and expensive task. Moreover, since the diffraction limit is reversely related to the frequency, a focused ultrasound piezo transducer of a few MHz has a focal diameter of ~ 4 mm that increases in the sub-MHz region [9]. Although high-frequency ultrasound has been used to improve the imaging spatial resolution, the propagating distance of the wave has been the limiting factor due to the strong attenuation in water and in biological tissue for the high-frequency component. A photoacoustic approach, employing pulsed optical excitation of photoacoustic materials or nano-absorber sandwiched with a polymer layer, results in ultrasound pulses with high amplitudes as well as high frequency. This minimizes the electrical components and cabling usually used in a traditional piezoelectric approach and creates new opportunities for the integration and miniaturization of optoacoustic devices operating in a broad frequency range.

The PA process is based on the thermoelastic effect, which depends on the optical absorption and the thermal expansion coefficient (β) of the material itself. In particular, the optical pulse, often a nanosecond excitation, induces a rapid heating and a transient expansion/contraction of the material with the emission of a sound wave. Recent advances in photoacoustic material have shown different devices made of a thin layer of light-absorber nanomaterial directly grown on a glass substrate, such as carbon nanotube (CNT) [10], carbon nanofiber (CF) [11], carbon soot nanoparticles (CSNP) [12], perovskite [13] and gold nanoparticle array [14]. In these devices, the nanomaterial layer was successively encapsulated with Polydimethylsiloxane (PDMS) used as a thermal-expanding layer. PDMS represents the primary polymer due to the high value of β and acoustic impedance comparable to water. Moreover, an acoustic cavity in a thin metal film/PDMS device or an

* Corresponding author.
*E-mail address:* daniele.vella@fs.uni-lj.si (D. Vella).

https://doi.org/10.1016/j.pacs.2022.100413
Received 15 July 2022; Received in revised form 16 September 2022; Accepted 7 October 2022
Available online 13 October 2022

extra-layer of gold nanoparticles in a carbon-material/PDMS structure has been introduced to increase the light-matter interaction [15] and to improve the PA conversion efficiency, which is often in the range of $10^{-3}$–$10^{-2}$ [10].

The high performance of these devices encounters a sophisticated fabrication process that is arduous to scale or is not flexible. Moreover, CVD growth of CNT requires high temperature, and this can also limit the choice of the substrate. An alternative way of preparation is represented by directly mixing PDMS with metallic particles or carbon filler (e.g., carbon black (CB)) [16,17]. However, to achieve the desired optical absorption, a high concentration of filler is used leading to material aggregation and a highly viscous solution. These compromise the uniformity of the film and control over the thickness leading to a much larger thickness than the light penetration depth, hence a spread of the ultrasonic pulse over time. In this regard, a simple preparation of a well-dispersed, controllable, and repeatable PDMS-based nanocomposite film is particularly of great interest and potential for integration with optical components, optofluidic chips, and shape-adaptive photoacoustic medical devices.

Two-dimensional graphene is a good candidate for absorbing nanomaterial due to its low density, high aspect ratio, and stability in many solvents without the need of surface functionalization [18–20]. Here, we report a single-laser-pulse excitation of a photoacoustic nanocomposite made of a few layers of graphene nanoflakes (FLG) and a PDMS polymer matrix. The nanoflakes were dispersed into the PDMS and spin-coated on the PDMS substrate to create a thin film with high optical absorption. For this purpose, a controlled protocol was developed to obtain well-dispersed FLG into the polymer at different weight percentages, ranging from 0.7 wt% to 1.1 wt%, and with different values of optical density (up to 94 % light absorbed and less than 2 % of scattered light, thickness of 17 μm). The measured ultrasonic wave achieves a maximum amplitude of 11 MPa in the planar configuration at the maximum laser fluence of ~228 mJ/cm$^2$. We observe that the signal amplitude linearly depends on the laser fluence, and it shows an onset of saturation at high laser fluence. Our observations can be interpreted as variations of the Grüneisen parameter with increasing temperature. We further demonstrate that a freestanding FLG composite can easily be embedded in an optical lens to launch spatially and temporally confined high amplitude ultrasonic wave (estimated >40 MPa) with a central frequency of 11 MHz and − 6 dB-bandwidth of 21.5 MHz. The time-dependent imaging of the process reveals the formation of cavitation microbubbles in water and in agar phantom. This highlights the possible implications of using the flexible photoacoustic composite in biomedical and biochemical applications.

## 2. Materials and method

### 2.1. Materials

The PA transducer was a composite of graphene nanoflakes and PDMS, the fabrication procedure is illustrated in Fig. 1a. Graphene nanoflakes in powder form (ACS material LLC - thickness 0.6 −1.2 nm) were added to Hexane solvent. Three samples with different weights 7, 9, and 11 mg respectively were dispersed in 3 ml of hexane using soft sonication for 20 min. In a separate vial, we mixed mechanically 1 g of PDMS (Sylgard 184) and 1 ml of Hexane. This content was transferred into the vial with FLG + Hexane, as an initial dispersion. After a manual mixing, the final FLG/PDMS/Hexane mix was transferred to the ampoule of the rotary evaporator. One more extra ml of hexane was used to wash any residual in the vial and added to the final solution. The total composite made of FLG, 1 g PDMS and total Hexane 5 ml was continuously mixed in the rotary evaporator keeping the vacuum with a water pump and soft sonication in a bath Elmasonic P30H (power level 40, frequency 80 kHz). The temperature of the bath was kept below 30 degrees by adding ice to the ultrasonic bath. After adding the cross-linker and spin coating the composite on a substrate, we noticed a not uniform film and that the polymer did not solidify after annealing. This could be related to an increasing temperature in the ultrasonic bath. The desired final volume (2 ml) was marked, and the process stopped after the partial evaporation of the solvent. The agitation/sonication process takes indicatively 2 h. The composite was then stirred overnight. Successively, after a quick sonication for 15 min, the cross-linking agent or curing agent was added in the ratio of 1:10 followed by 30 min of stirring. The composite was spin-coated at different velocities (initial step 30 s at 500 rpm second step ranging from 2 krpm to 7 krpm) on PDMS substrate 1.5 mm thick. After allocating the samples in the vacuum bell

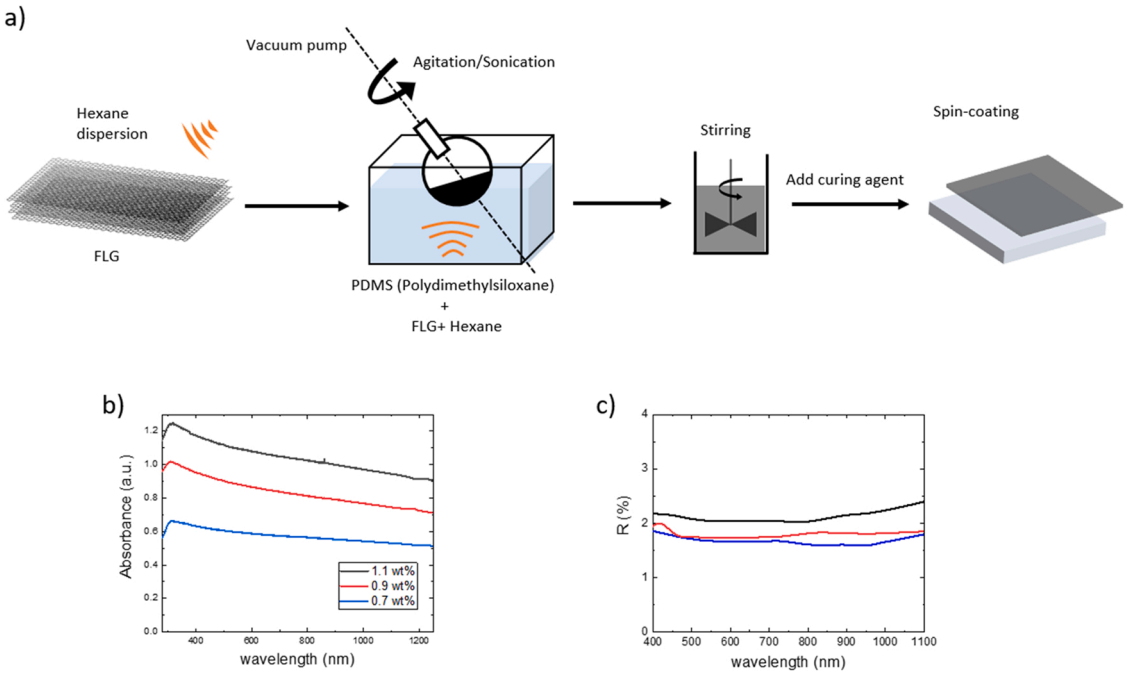


**Fig. 1.** a) Representation of the experimental protocol for the fabrication of the polymer composite film. b) Absorbance of the film for different concentrations of FLG in the composite. c) Scattering spectra of the at different concentrations, the color lines follow the same legend in b).

($10^{-3}$ mbar) for 40 min, they were cured at 80 °C for 1 h. The PDMS substrate was prepared by mixing the curing agent in the ratio of 1:10, degasification, and cured at 150 °C for 1 h.

The substrate used for the preparation of the photoacoustic focusing lens was a commercial ultraclean PDMS Gel-Pak X4 (165 μm thick), often used for transferring two-dimensional transition metal dichalcogenides [21]. The procedure to deposit the composite was the same as described above. However, after curing the composite on a flexible PMDS (mounted on a glass slide), the entire structure was flipped over and an additional thin layer of PDMS was spin-coated on its backside. This layer acts as an adhesive layer at the surface of the plano concave lens (12.7 mm diameter, 12.9 mm radius of curvature, Thorlabs LC1054). The stack with the uncured layer was manually aligned with the lens and released. The vacuum condition in the chamber ($10^{-3}$ mbar) promoted the adhesion of the film on the lens surface. The last step of the protocol was the curing of the adhesive layer that fixes the stack to the lens surface. The result is a shape-adaptive photoacoustic film that can stick to a more complex-shape sample. The lens was used over several thousand pulses in the cavitation regime without visible damage or detachment of the film.

The thickness of the films was measured using a Bruker Dektak XT profilometer in a soft contact mode, for all FLG concentrations and different spin velocities. The measured thickness as a function of the spin velocity, varying from 5 μm to 22 μm, was nearly similar for all the concentrations (see Fig. S1, suppl. Inf.).

The transmittance (T) and reflectance (R) from the samples were collected with a UV–Vis spectrophotometer Perkin Lambda 1050 equipped with an integrating sphere module. The resolution was 1 nm. The absorbance of the film was measured in transmission geometry following the Beer-Lambert law and using a portion of the substrate on the same sample as a blank reference, that was covered with Kapton tape before spin-coating the composite. The scattering of the film with respect to the PDMS substrate was measured within an integrating sphere in reflection geometry. For the estimation of the % of absorption (A = 1-T + R), that appears in the estimation of η (conversion efficiency), T and R were measured considering the entire structure, film plus approximately 1.5 mm thick PDMS substrate.

Commercial culinary agar was mixed with degassed distillate water in a weight ratio of 2 %. The solution was heated in the microwave for 30 s and gently mixed. This cycle was repeated until the solution turned transparent. Afterward, it was poured into a rectangular glass box and placed in the refrigerator at 4 °C to solidify.

### 2.2. Experimental setup

The experimental setup is presented in Fig. 2. The PA transducer was immersed (5 mm below the water surface) in a glass bath containing distilled water. A Q-switched Nd:YAG laser source with 12 ns pulse duration (StarWalker, Fotona d.o.o.) was used as an excitation source in single pulse mode. The laser output and the number of pulses are controlled via software giving a single shoot output each second. The laser fluence was adjusted by controlling the polarization of the light with a half-waveplate and a polarized beam splitter. The laser spot size was 8 mm. We employed a Schlieren imaging system to monitor the wave propagation in water and in agar phantom. The imaging detection system is composed of an 8 ns flash illumination lamp (NANOLITE HSPS flash lamps) that is collimated through an achromatic condenser lens and successively focused on the sharp edge of a razor (knife-edge), placed perpendicular to the beam between the imaging lens and the CCD camera (Point Gray, monochrome Flea3, 1280 × 1024 pixel). The laser pulse was detected with a Si-photodiode (Thorlabs, DET10A) and used as a reference trigger input for the delay generator (Tektronix AFG3102), which upon receiving the trigger input from the photodiode, generates a signal output to trigger the ns flash lamp with an adjustable delay relative to the laser excitation. The CCD camera shutter opens temporally before communicating with the laser system. The light coming from the excitation laser (1064 nm) was filtered by using a short pass filter before the CCD camera to prevent its overexposure. The ultrasonic wave was detected through a hydrophone needle 200 μm diameter (Precision Acoustic LTD) placed 5 mm from the PA transducer. The hydrophone position was controlled by a manipulator (X, Y, Z) to measure the distribution of the pressure amplitude.

## 3. Results and discussion

### 3.1. Photo-thermal-acoustic conversion

Ultrasound waves generated from the interaction between light and thermoelastic material require a short laser pulse to satisfy the stress confinement condition [10]. Photoacoustic generation in graphene is wavelength-independent due to the nature of its band structure. In Fig. 3a is sketched the photoacoustic conversion. Optical transitions in the Dirac band of graphene take place upon photoexcitation [22]. The photon energy is converted into phonon population during the fast electron relaxation on the picosecond timescale [23–25], which occur

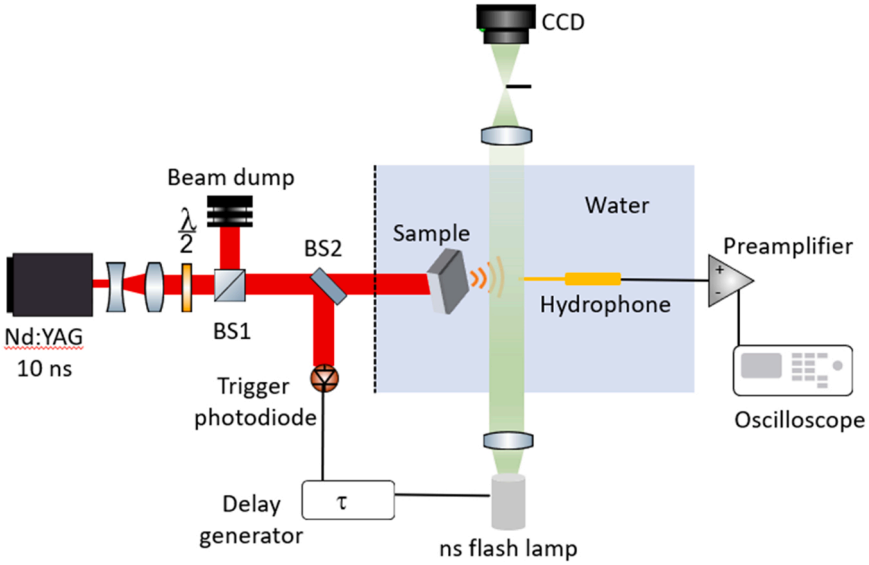


**Fig. 2.** a) Schematic of the experimental setup employed for the photoacoustic measurements.

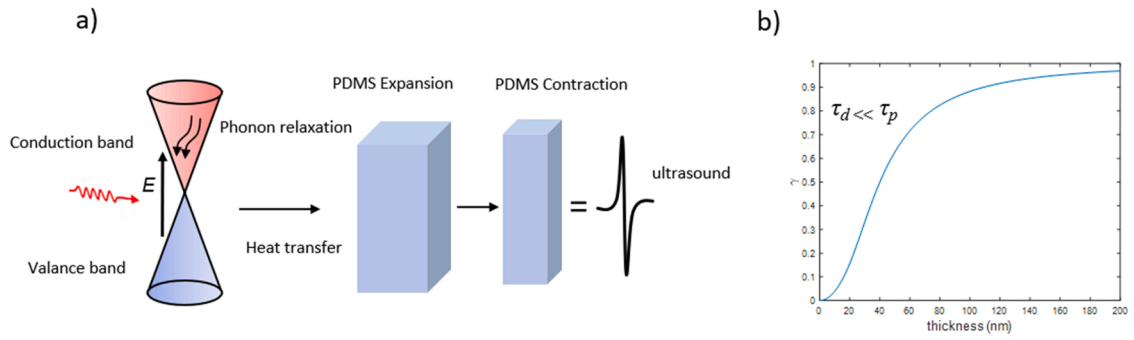


**Fig. 3.** a) Sketch of the photoacoustic process in FLG/PDMS composite upon laser pulse excitation. b) portion of heat transfer γ as function of the thickness of the graphite absorber.

via non-radiative electron-phonon scattering. This thermal energy of the lattice is immediately dissipated towards the surrounding medium (PDMS) that expands and contracts to generate a pressure wave, like in a piston.

Hence, a fast heat transfer from the nanomaterial to the surrounding environment is extremely important for photoacoustic conversion. The photothermal process gives rise to an increasing temperature ($\Delta T$) in the nanoobject that is proportional to the volumetric energy deposition and depends on the fraction of thermal energy remaining in the absorber ($\gamma$), as follows [26]:

$$\Delta T = \frac{F\mu\gamma}{\rho c_p} \tag{1}$$

Where $F$, μ, $\rho$, and $c_p$ are the laser fluence, linear absorption coefficient, density, and specific heat capacity, respectively. The fraction of the heat transfer $\gamma$ after the pulse duration $\tau_p$ depends on the heat diffusion time $\tau_d$ in the nanomaterial:

$$\gamma = \frac{\tau_d}{\tau_p} \times \left(1 - e^{(\tau_p/\tau_d)}\right) \tag{2}$$

For a nano-absorber with plane geometry, the characteristic heat diffusion time, expressed as $\tau_d = z^2/2D$, where $D$ is the thermal diffusivity of PDMS and $z$ the thickness of the FLG, is on the order of a few tens of picoseconds. Therefore, in a few layers, $\tau_d$ is much smaller than the laser pulse duration, and all the thermal energy is then quickly transferred to the PDMS and converted to mechanical energy due to its high thermal expansion ($0.96 \times 10^{-3}$ 1/K). The negligible energy that remains in the ultra-thin absorber (0.6 −1.2 nm thick) and the high thermal expansion coefficient of the polymer are the key factors in photo-thermal acoustic conversion. Hence, thermoacoustic pressure is dominated by the surrounding PDMS, which undergoes a volumetric expansion, and the superposition of each contribution originates from multiple sources of individual emitters in the composite. The curve in Fig. 3b shows the crossover towards a heat confinement condition with increasing the thickness of the absorber according to Eq. (2). For thickness up to 20 nm $\gamma$ is below 10% but by increasing the number of layers (thickness >120 nm) $\gamma$ becomes higher than 90 % and $\tau_d > \tau_p$. This causes a slower heat transfer process towards the expander element. Analogously, different geometry of a carbon-nanomaterial such as CNT follow the same trend but reaches a value of $\gamma > 99$ % for a tube diameter of ~ 1 μm [27]. This interface aspect is important during the design of the photoacoustic source and can be applied to other systems made of mechanically exfoliated or growth-layered materials.

However, for a composite where the absorber is dispersed into the expander the rapid exchange of heat at the interface and high light absorption are not the only important aspect of the photoacoustic response. From theory, the produced photoacoustic waveform depends on the light absorption profile that can be approximated as $\tau_p + 1/c_p\mu$ [10]. The effective thickness of the composite (absorber/expander) is then represented by the light penetration depth that influences the characteristic of the emitted sound wave. Indeed, a thickness of the composite much larger than the penetration depth will cause acoustic attenuation. We will show that the photoacoustic frequency response of the composite with the nanosecond excitation depends on the dimension of the source (effective thickness or penetration depth), suggesting a scenario closer to the short pulse regime [20].

### 3.2. Photoacoustic of the composite film

The concentrations of FLG in the composite chosen for this study were 0.7 wt%, 0.9 wt%, and 1.1 wt%. These amounts combined with different spin-coating velocities induce modification of the optical absorbance that can vary from 0.3 to 1.3, refer to Fig S2a in suppl. inf. that summarizes the absorbance at 1064 nm excitation wavelength as a function of the thickness. Increasing the spin-coating velocity from 2 krpm to 7 krpm the absorbance decreases while retaining its line shape. To generate a sizeable variation in pressure an absorption > 60 % has generally been used in previous research works. The absorbance spectra (or optical density, OD = -log ($T_{film}/T_{PDMS}$)) for the 17 μm thick sample at different FLG concentrations are shown in Fig. 1b. To check the optical quality of the film, we measured the amount of scattered light collected within the integrating sphere which reveals a scattering component of around 2 %, see Fig. 1c. It is worth mentioning that the cross-sectional SEM image of the film, although highly conductive with respect to bare PDMS, did not reveal the nanoflakes due to the ultra-thin thickness and presumable parallel preferential orientation.

The flat sample was immersed in distilled water and irradiated with a single ns laser pulse (see method section for experimental details) over an area of 8 mm diameter. Upon photoexcitation, ultrasonic waves are launched in water and in opposite direction through the PDMS substrate. The waveform shown in Fig. 4a, is characterized by a prominent positive pressure peak and a much less intense negative pressure peak. A similar profile has been observed in other work where carbon nanomaterials encapsulated with a polymer layer were excited through a similar irradiated area [12]. The traveling wave derives from the superposition of secondary spherical wavelets, originating from multiple sources of individual nano-emitters. A Schlieren image of the traveling wave is depicted in the insert of Fig. 4a. The pressure amplitude increases following the trend of the absorbance profile for different film thicknesses (see Fig. S2 suppl. Inf.). Hence by increasing absorbance, a composite thickness (~17 μm) moderately larger than the light penetration depth generates higher pressure without introducing acoustic attenuation.

The frequency domain of the signal in Fig. 4b shows a − 6db bandwidth of ~14 MHz and a center frequency of around 6 MHz. The comparison with different wt% and same thickness reveals a small shift of both peak position and − 6db bandwidth towards higher frequency, which correlates with the difference in penetration depths ($\delta$) or effective thickness. For the samples, 0.7 wt%, 0.9 wt%, 1.1 wt%, the $\delta$ was

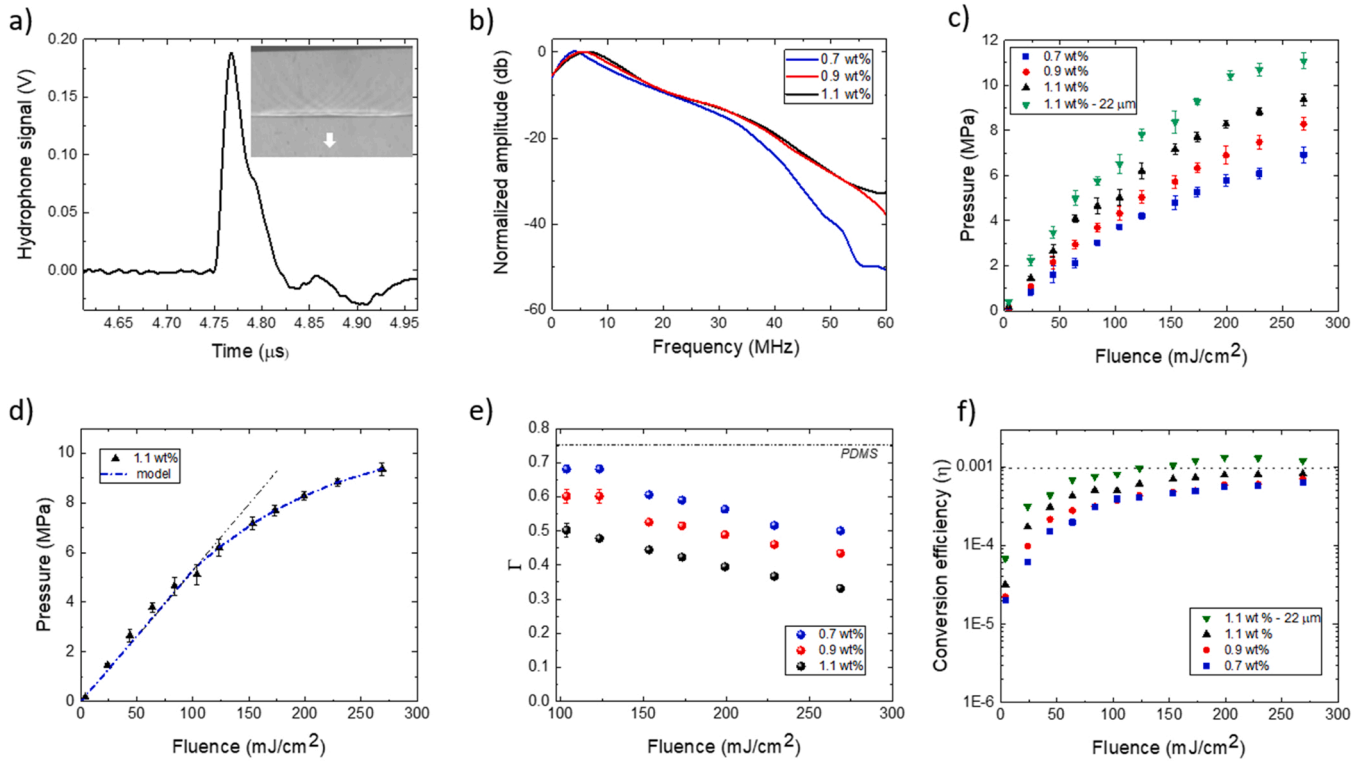


**Fig. 4.** (a) Pressure wave profile recorded with needle hydrophone. Insert shows the Schlieren image of the propagating wave (sample 0.9 wt%, 17 μm thick). (b) Normalized amplitude of the frequency spectrum for the three concentrations of FLG and the same film thickness (17 μm). (c) Positive pressure peak as a function of the laser fluence. (d) Positive pressure peak for the 1.1 wt% sample (black dot) and fit from the model in Eq. (3) (blue curve). (e) Γ evaluated from the fit as a function of the laser fluence. The first value comes from the fit of the linear part of the data points. (f) Conversion efficiency η estimated for different laser fluence and different FLG concentrations.

13.5 μm, 10 μm, and 7.6 μm respectively and small variations are expected. Indeed, a few MHz shifts of the frequency (from 1 MHz to 5 MHz) has been seen in CNT polymer composite varying the concentration of the nano-absorber from 2.5 to 10 wt%, hence decreasing $\delta$[9]. This identifies the light absorption profile as the main contribution to the effective thickness of the system absorbing / expanding layer.

The dependency of the acoustic peak pressure from the laser fluence is shown in Fig. 4c. The pressure increases with the fluence and follows the same trend for all the FLG concentrations. The signal reaches 9.5 MPa for 1.1 wt% of FLG at 270 mJ/cm$^2$. For comparison, the highest achievable pressure (11.5 MPa) is generated using the thicker film (22 μm or 2 krpm spin-coating velocity) of the same concentration (1.1 wt%), due to the increased absorption. The photoacoustic amplitude depends on the thermal energy transfer and increases linearly with the absorbed fluence $P \propto \gamma AF$ [28]. However, in Fig. 4c the linear behavior becomes sublinear after 120 mJ/cm$^2$, and the onset of saturation is seen when increasing $F$ up to 270 mJ/cm$^2$.

Saturation of the PA signal was attributed either to the limit of the hydrophone bandwidth or the degradation of the absorbing layer at much lower laser fluence or not discussed at all [8,12,15]. Here, we excluded the limitation of the hydrophone since saturation of the pre-amplifier takes place at 16 MPa. Further, we did not observe any degradation or detachment of the film within the range of our measurements that were repeated multiple times. Ablation of the film and vapor bubbles formation was instead observed for laser fluence around 300 mJ/cm$^2$ and above, likewise in the CNT-PA lens [27].

The sublinear behavior with increasing laser intensity can be explained by considering the pressure amplitude generated from the thermal expansion, defined as follows:

$$P = \Gamma\left(1-\gamma\right)A\frac{F}{\delta} \tag{3}$$

Where $\Gamma$ is the Grüneisen parameter, (1-$\gamma$) is the fraction of thermal energy that is transferred from FLG to PDMS, $A$ (%) is the absorption taking into account the transmitted and reflected light ($1\text{-}T + R$) from the entire structure, $F/\delta$ is the energy volume density considering the light penetration depth. Hence the pressure is linear with the fluence, and all the parameters are properties of the PA lens itself. In this specific case, $\gamma$ is negligible as we mentioned in the previous section, $A$ increases with FLG concentrations respectively of 67 %, 71 %, and 80% for the samples presented in Fig. 4c (see optical spectra in Fig S3 a, b suppl. Inf.), and the Grüneisen parameter encompasses the volumetric thermal expansion $\beta$, speed of sound $c$, and specific heat capacity $c_p$ that are related as $\Gamma = \beta c^2/c_p$. It can be seen that $\beta$ and $c_p$ are temperature-dependent and then also the photoacoustic response. We ascribe the saturation in the photoacoustic amplitude to the decreasing of the Grüneisen parameter due to an increasing temperature.

In the linear regime (up to 120 mJ/cm$^2$) the pressure data points were fitted to Eq. (3) with $\Gamma$ free parameter, the slope of the curve (Fig. 4d). While in the non-linear region, the decreasing of $\Gamma$ for each new increment of $F$ was evaluated to reproduce the PA amplitudes. The results of the fit are shown in Fig. 4e. The starting values of $\Gamma$ represent the slope of the linear fit and scale with the wt%. For comparison $\Gamma_{PDMS} = 0.72$ is also displayed as a reference. Indeed, the introduction of graphene filler in the polymer matrix affects both $\beta$ and $c_p$ and it should be taken into consideration when the absorber and expander are in a composite.

The $c_p$ has been shown to decrease by introducing carbon inclusion up to 10 wt% [29], as well as $\beta$ parameter also undergoes a reduction due to the network of the filler that blocks the volume expansion. The latter is supposed to be on the order of 20 % and 30 % smaller in carbon nanofiber and tubular graphene PDMS-based structures [30,31]. An estimation of $c_p$ is given in Section 4 of the suppl. inf. as a weighted

average with respect to the wt% of FLG and PDMS. The small scaling of $c_p$ from 1.46 kJ/kg K (PDMS) to 1.45 kJ/kg K (1.1 wt%) could not explain the decrease of $\Gamma$, which is mainly affected by the change in $\beta$. In the Supplementary information, a rough estimation of $\beta$ from the fit is given that corroborates previous findings (see Fig. S4). However, the increasing temperature for $F$ higher than 120 mJ/cm$^2$ (see Supplementary information Section 6) leads to a decrease of $\Gamma$ that can be mainly related to the change of $c_p$. In fact, for a wide range of curing temperatures the coefficient of thermal expansion in pure PDMS is either constant or slightly increases when mixed with carbon nanomaterials [32,33], while $c_p$ increases rapidly with temperature. Observation of monotonically increasing $c_p$ in CNT or graphene composites can support the hypothesis that $\Gamma$ drops because the growth of $c_p$ is dominant [34,35].

The saturation of the peak pressure also affects the photoacoustic conversion efficiency ($\eta$) that theoretically should be also linear with the laser fluence. It is calculated as a ratio between the acoustic energy, $E_a = 1/\rho c S \int P^2(t)dt$(S area of laser facula), and the absorbed optical energy $AE_{opt}$. The values are shown in Fig. 4 f. Although the composite has a high damage threshold, the maximum achievable value for the 80% absorbed film is between 1 and 1.3 × 10$^{-3}$ for $F$ above 140 mJ. Similar values have been achieved in devices made of directly grown nano-absorber layers encapsulated in PDMS but at lower fluence. This can be seen in Table 1 which summarizes the characteristics of ultrasound emitters based on PDMS, carbon nanomaterials, and metallic film or nanostructure. The frequency response is comparable with other carbon-based materials measured with the same needle hydrophone although the laser pulse excitation in this work was two times longer. The film can stand relatively higher fluence in comparison with CSNP/PDMS which starts to deteriorate after a few mJ/cm$^2$, and it generates a relatively high-pressure peak, superior to the metallic structure and greater than CNT/PDMS previously reported [20]. The highest positive peak pressure for carbon-based composite is reported for CNT yarn/PDMS, however, FLG/PDMS (planar configuration) shows a pronounced negative peak pressure of around 2.5 MPa (see data point in Fig. S5, Supplementary information). These comparisons are indicative because the fluence in Table 1 is an absolute value, that does not indicate the absorbed fluence, which can vary depending on absorption. In some research, this fluence represents the highest value before degradation of the composite. Moreover, the increasing pressure could be boosted by the device geometry, e.g., multiple reflections of the laser light or wave superposition effect, which is not specified and can be deduced from the references.

### 3.3. Focusing PA lens

A strategy to increase the PA amplitude at lower $F$ is to consider a focusing configuration and the amplification gain. We implemented a photoacoustic lens starting from the concepts of flexibility and

**Table 1**
Characteristics of ultrasound emitters using PDMS composite. Acronyms for carbon-based composite are indicated in the main text. AuNP: gold nanoparticle; Cr: chromium film. The asterisk symbol (*) indicates that this is the only information reported and it was not possible to calculate the fluence. The tilde symbol ''∼'' means that the values were estimated from the plot. The dash symbol ''-'' means that the values were not reported.

| Author | Material | Coated substrate | Aperture [mm] | Thickness [μm] | Focal [mm] | Detector-distance [mm] | $P^+/P^-$ [MPa] | $f_c$ [MHz] | -6 db [MHz] | Fluence [mJ/cm$^2$] | $\tau_p$ [ns] | η x 10$^{-3}$ |
|---|---|---|---|---|---|---|---|---|---|---|---|---|
| *Chang* et al. [12] | CSNP/PDMS<br>CF/PDMS<br>CB/PDMS | glass slide | 10 | 25<br>57.8<br>30 | | needle hydrophone - 5 | 4.8/∼0.75<br>2.3/-<br>0.8/- | 10<br>-<br>- | 21<br>10<br>12 | 3.57 | 6 | 4.41<br>1.66<br>0.34 |
| *Hsieh* et al. [36] | CF/PDMS<br>CB/PDMS | glass slide | 12 | 58<br>30 | | needle hydrophone - 3.65 | 12.15 /∼1<br>1.6/- | ∼ 2.5 ∼ 2.5 | 7.63<br>7.84 | 3.71 | 6 | – |
| *Buma* et al. [16] | CB/PDMS | glass slide | – | – | | needle hydrophone - 10 | 0.15/- | – | – | 10.4 | 20 | – |
| *Baac* et al. [37] | CNT/PDMS<br>AuNP-array | fused silica | 19.6 | 2.6<br>30 nm | | optical microring - 1.4 | – | – | ∼80<br>∼80 | 3(*)<br>[mW/cm$^2$] | 6 | – |
| *Silva* et al. [20] | Functionalized-CNT/PDMS | glass slide | 8 | 38 | | a) needle hydrophone - 3<br>b) contact transducer | ∼0.4/<br>∼0.05<br>- | – | -<br>80 | 50<br>50 | 8 | – |
| *Chen* et al. [15] | CNT yarn/PDMS | flat PDMS | 5 | 5 | | needle hydrophone - 5 | 19/∼ 1 | 9.3 | – | 45 | 6 | 8.6 |
| *Colchester* et al. [38] | Functionalized-CNT/PDMS | core optical fiber | 105 μm<br>200 μm | – | | needle hydrophone - 2 | 0.45/-<br>0.9/- | – | 12<br>15 | 41.6<br>36.3 | 2 | – |
| *Noimark* et al. [39] | Functionalized-CNT gel/PDMS | core optical fiber | 200 μm | – | | needle hydrophone - 3 | ∼0.8/<br>∼0.56 | 19.4 | 29.2 | 33.1 | 2 | – |
| *Lee and Guo*[40] | PDMS/Cr/PDMS Al-reflector | glass slide | – | < 1 | | PVDF - | 1.82/- | – | – | 2.35 | 6 | 0.42 |
| *This work* | FLG/PDMS | flat PDMS | 8 | 22 | | Needle hydrophone - 5 | 11/2.5 | 7 | 15.6 | 228 | 12 | 1.3 |
| *Lee* et al. [41] | CNT/PDMS | Concave lens | 15 | – | 9.2 | Fiber-optic hydrophone - 9.2 | ∼ 60/∼ 26 | – | 25 | 6.8 | 6 | – |
| *Baac* et al. [8] | CNT/PDMS | Concave lens | 6 | 16 | 5.5 | Fiber-optic hydrophone - 5.5 | 22/10 | 15 | 20 | 42.4 | 6 | – |
| *This work* | PDMS/FLG-PDMS | Concave lens | 8 | 165/17 | 13 | Needle hydrophone - 13 | 29/12 | 11 | 21.5 | 40 | 12 | – |

adaptability of PDMS on the concave surface. For this purpose, we spin-coated two layers on a commercial viscoelastic ultraclean flat substrate used in microelectronic: the 0.9 wt% FLG composite (17 μm), and on the backside of the substrate a thin layer of PDMS used as an adhesive layer on the surface of the concave lens (sketch in Fig. 5a, see details in material and method). The film under vacuum conditions and annealing completely follows the lens curvature without suffering any damage or detachment for $F < 300$ mJ/cm$^2$. In this way, the acoustic pressure is confined and reaches the highest amplitude at the focal point, located at ~13 mm from the PA lens (clear aperture of 10 mm). The amplification factor of the lens, or acoustic gain $G$, is defined as the ratio of the pressure in the focus compared to the pressure close to the lens surface:

$$G = \frac{2\pi f}{c_0} r \left(1 - \sqrt{1 - \frac{1}{4f_N^2}}\right) \quad (4)$$

Where $c, f, r, f_N$ respectively are the speed of sound in water, the pressure wave frequency, the radius of curvature, and the f-number of the lens. In this case, the transient pressure has a central frequency of 11 MHz and $f_N = 1.4$. Considering the attenuation in water ($2.2 * 10^{-3}$ db/cm/MHz) that depends on the acoustic frequency $\propto f^2$, the estimated gain is approximately $G$ ~36. The measured signal in Fig. 5a on the right panel shows the pressure at 6 mm from the lens and the amplified pressure at the focal point.

The propagating pressure is made of a wave launched in the forward direction, and a backward wave reflected at the glass-PDMS interface, clearly visible in the Schlieren image of Fig. 5d. The maximum pressure signal at the focus was found with the help of the imaging system and by scanning the hydrophone needle in the $z$-direction (axial). The pressure waveform shown in Fig. 5b, is characterized by a strong positive peak and a longer trailing of the negative peak pressure. Deviation from the time-derivative of the Gaussian pulse was mainly attributed to a non-linear propagation of the finite-amplitude pulse[8]. The frequency spectrum of the signal reveals a $Bw_{\text{-6b}}$~ 21.5 MHz (Fig. 5c). This simple fabrication method enables to reach similar performance observed in other PA devices, realized with more sophisticated approaches. Table 1 shows a photoacoustic lens with similar $f_N$ (> 0.9) realized with direct grown CNT and PDMS [8] having similar characteristics.

The spatial confinement of high pressure and high-frequency ultrasound in a small spot for therapeutical purposes is of great interest and requires knowledge of beam quality in the focus. The radial dimension of the focal spot was measured by scanning the needle hydrophone in the lateral and longitudinal directions. Fig. 5d shows the positive peak pressure at the focal point as a function of the position. The distribution in each direction was fitted to a Gaussian curve to evaluate the full-width half-maximum that gives the widths of 220 μm (lateral) and 364 μm (longitudinal). Their ratio σ defines the degree of ellipticity of the focal dimension, which in this case is ~ 0.60. Hence higher is the value of σ, the closer to a spherical shape is the focal spot. This number is relatively high if compared with CNT grown on a concave lens, where the σ scales down with increasing f-number, reaching the maximum value of 0.45 for f-number of 0.61, and a value of ~ 0.15 for lens geometrically similar to the lens here considered [41].

The pressure peaks were measured up to 40 mJ/cm$^2$ to avoid damage to the needle hydrophone. A spatial averaging effect due to the finite size of the hydrophone (effective radius of 100 μm) was included for the correction of the data points (see suppl, Section 7). The initial linear relation starts a saturation process above 30 mJ/cm$^2$, see Fig. 5e. From

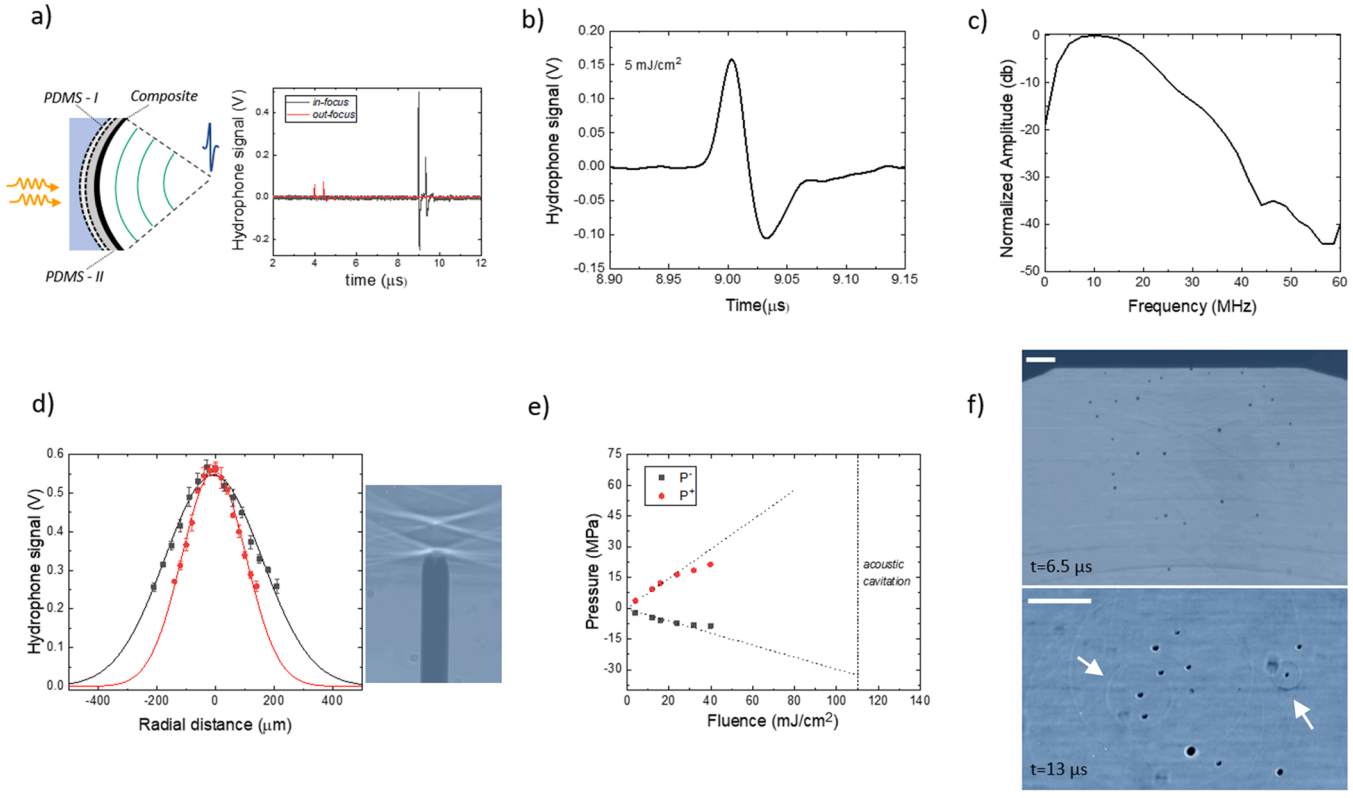


**Fig. 5.** (a) Illustration of the PA lens composition (left panel) and pressure signals recorded separately close to the lens and in the focal point (right panel). (b) Pressure signal measured in the focus at laser fluence of 5 mJ/cm$^2$, 0.9 wt% FLG. (c) Normalized amplitude of the frequency spectrum of the signal in b). d) Distribution of the positive peak data points (primary wave) in focus and close to it, recorded by scanning the hydrophone in the lateral and longitudinal directions. The solid line is the Gaussian fit of the data points. Besides, Schlieren image of the focusing wave on the focal region: primary wave and back-reflected wave, hydrophone aperture is 200 μm. e) Recorded positive and negative peak pressures in focus for different laser fluence. f) Schlieren image of the acoustic cavitation after the passage of the ultrasonics front wave (upper panel). Bottom panel: example of observed collapses of the cavitation microbubble and shock wave (indicated with white arrows) emission at a laser fluence of 220 mJ/cm$^2$. The scale bar is 1 mm.

our previous observations in the flat sample, we can rule out the temperature-induced changes since the linearity is still preserved within this range of laser fluences. Here, the observed saturation of the pressure reflects the saturation of the preamplifier (800 mV) that limits the maximum measurable pressure to ~16 MPa, after this value the hydrophone response is nonlinear, and damage can also occur. In another work, employing the same sensor, similar results were also reported [15]. However, since the PA response of the composite is linear with $F$ a prediction with a linear fit up to 110 mJ/cm$^2$ shows an achievable negative pressure of ~ - 30 MPa. Our observation was corroborated by monitoring the formation of cavitation bubbles in distilled water that usually form at a negative pressure of around ~ − 27 MPa[42]. Indeed, at a laser fluence of 110 mJ/cm$^2$ and above cavitation inception occurs along the axial direction of the lens. Schlieren images of the acoustic cavitation in two different time intervals are shown in Fig. 5f.

The positive peak pressure most probably exceeds 40 MPa (laser fluence > 55 mJ/cm$^2$), and the linear fit could give an overestimation at high laser fluences. In fact, a further increase of the laser energy produces excessive positive peak pressure that experiences a robust acoustic attenuation in water for the high-frequency components. This led to the saturation or change of the slope that manifests at amplitude above 40 MPa [41].

### 3.4. High-frequency cavitation and implications

Acoustic cavitation is generally defined as the transient pressure that induces rupture of the liquid and the formation of dispersed cavities behind the pressure front. However, due to the inhomogeneity of all the liquid, acoustic cavitation is also related to the presence of dissolved gasses and microscopic gas bubbles that lower the tensile strength of the liquid. In the presence of a transient pressure, the pre-existing gas bubble can pulsate and grow, or microbubbles start to form on gas nuclei [43,44]. During their life cycle cavitation bubbles undergo expansions and shrinkages via rectified diffusion and it ends with the emission of multiple shock waves that lead to a severe secondary pressure gradient [45,46] (see Fig. 5f bottom panel). Therefore, the focusing geometry and the high gain enable the possibility to achieve cavitation in the free field although the lens has a relatively larger focal distance and higher f-number compared with previous works. In cavitation therapy, this can be a challenge since the free-field cavitation at high frequencies requires a higher pressure threshold $P \propto f^{\frac{1}{2}}$ [47]. This threshold can change in clinical application depending on the structure and morphology of the tissues [10].

The cavitating regime was also observed in tissue-mimicking-material, particularly agar gel was chosen as a propagating medium. Largely used in preclinical studies of wave-tissue interactions for therapy [48,49], imaging [50,51] or as an acceptor layer in cavitation-based transdermal drug delivery [52], this water-based phantom exhibits elastic properties similar to soft tissues, such as skin [49]. It is nearly transparent in the visible range allowing the observation of wave propagation and cavitation bubbles in our experiment. Its physical parameters including the velocity of the ultrasonic wave ~ 1.46 km/s [49], acoustic impedance similar to that of water (~1.5 MRayl) [53] and an acoustic attenuation that can rank from 0.04 to 1.4 dB/cm/MHz, ~ 0.4 dB/cm/MHz for ~ 2 wt% of agar at around 5 MHz [53,54], are close to many soft tissues [51,54–57], making this material a reasonable in-vitro approximation. Cross-sectional images of the agar phantom irradiated with the ultrasonic pressure wave at three different time sequences are shown in Fig. 6. The lens approaches the agar surface and water is within the space delimited by the gel surface and the lens curvature. The high amplitude ultrasonic wave, characterized by a rapid pressure jump, propagates through the agar leading to the growth of microbubbles along the direction of propagation (Fig. 6b,c) up to the focal point. A laser fluence of 200 mJ/cm$^2$ is sufficient to induce many cavitation events whose spatial distribution in the lateral direction follows the pressure field, reducing with the depth. A smaller spatial distribution of microbubbles is shown in the Supplementary information (Section 8), where the lens is positioned far from the agar surface and the focus is a few mm below the gel surface.

Our observations shed light on the possibility to generate high amplitude PA pulse and transient cavitation within the soft tissue that could be used for localized ablation. In principle, shaping the PA lens with a shorter focal distance could reduce the exposed area and lead to a more localized pressure field and cavitation as well. Further, high-frequency ultrasounds and cavitation play an important role in the transdermal drug delivery [58,59], permeabilization of the cell membrane [60], and release from drug-loaded nanoparticles [17]. Sonophoresis devices usually employ low-frequency (hundreds of kHz) and high-frequency ultrasound (1–16 MHz), depending on the application, that facilitate the transport through the epidermis, stratum corneum, of therapeutic agents. The permeability enhancement of skin is mainly caused by the presence of acoustic cavitation inside the skin, or the joint action of cavitation at the skin interface and microjet penetration during the bubble collapses, which create a structural disorder in the lipid region of the stratum corneum [61,62]. Laser-induced ultrasound and acoustic cavitation using PA film of graphene-PDMS composite on flexible substrate allow potential applications in this field.

## 4. Conclusion

We studied the photoacoustic response of graphene-PDMS composite when the absorber is dispersed in the polymer matrix. Two operating configurations were considered: planar and focusing. A protocol to well disperse graphene nanoflakes in the PDMS matrix was developed to create PA film with different concentrations of graphene up to 1.1 wt%. We find that the photoacoustic response scales up with optical absorption reaching 11 MPa at the laser fluence of ~ 228 mJ/cm$^2$. The increase of FLG concentration, hence the decrease in penetration depth, stretches the frequency spectrum toward higher values. The PA amplitude deviates from the linear behavior increasing the laser fluence, which indicates a decrease of the Grüneisen parameter with temperature most probably due to the dominant effect of the composite specific heat.

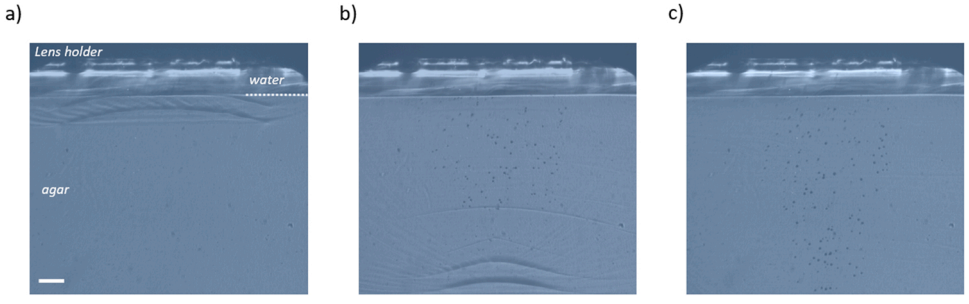


**Fig. 6.** (a) Schlieren images of the propagating wave and acoustic cavitation in agar gel at time delay $t_0 = 2$ μs. (b) at $t_1 = 5.5$ μs. (c) $t_2 = 7.5$ μs. The scale bar is 1 mm.

Other possible effects that can lead to a sublinearity such as bandwidth saturation of the sensor or detachment of the film were not observed in our experiments.

We further show the generation of spatially confined high amplitude (achievable $>$ 40 MPa, at laser fluence $>$ 55 mJ/cm$^2$) and high frequency (B-6db $\sim$ 21.5 MHz) ultrasonic wave, focalized over an area of a few hundred microns. This was achieved by embedding the freestanding film in an optical lens, and it could be also extended in rigid supports with a more complex shape. We observed that the high acoustic gain in the focusing geometry enables acoustic cavitation microbubbles in water and in agar phantom for moderate laser fluence. Our work highlights the potential of the PA flexible FLG/PDMS composite film, which could enable localized ablation therapy or sonophoresis-based drug delivery.

## Declaration of Competing Interest

The authors declare that they have no known competing financial interests or personal relationships that could have appeared to influence the work reported in this paper.

## Data availability

Data will be made available on request.

## Acknowledgment

We acknowledge Ministrstvo za Izobraževanje, Znanost in Šport (project LASPRO); Javna Agencija za Raziskovalno Dejavnost RS (core funding No. P2–0392, project funding No. L2–1833). We also acknowledge the CENN Nanocenter (Ljubljana, Slovenia) and thank for the financial support through the program group P2–0082 and Javna Agencija za Raziskovalno Dejavnost RS project no. J2–2509. We thank Fotona d.o.o for providing the laser source and technical support. We thank Dr. Victor Vega Mayoral for the discussion.

## Appendix A. Supporting information

Supplementary data associated with this article can be found in the online version at doi:10.1016/j.pacs.2022.100413.

## References

[1] L.V. Wang, Photoacoustic imaging and spectroscopy, 2009, 499. ⟨https://books.google.com/books/about/Photoacoustic_Imaging_and_Spectroscopy.html?hl=sl&id=QzdHEmUFcXgC⟩.
[2] N. Kuthirummal, Listening to nanomaterials: photoacoustic spectroscopy, J. Chem. Educ. 86 (2009) 1238–1240, https://doi.org/10.1021/ED086P1238.
[3] A. Sampaolo, P. Patimisco, M. Giglio, A. Zifarelli, H. Wu, L. Dong, V. Spagnolo, Quartz-enhanced photoacoustic spectroscopy for multi-gas detection: a review, Anal. Chim. Acta 1202 (2022), 338894, https://doi.org/10.1016/J.ACA.2021.338894.
[4] G. Thummerer, G. Mayr, M. Haltmeier, P. Burgholzer, Photoacoustic reconstruction from photothermal measurements including prior information, Photoacoustics 19 (2020), 100175, https://doi.org/10.1016/J.PACS.2020.100175.
[5] X. Wang, Y. Pang, G. Ku, X. Xie, G. Stoica, L. v Wang, Noninvasive laser-induced photoacoustic tomography for structural and functional in vivo imaging of the brain, Nat. Biotechnol. 21 (2003) 803–806, https://doi.org/10.1038/nbt839.
[6] J. Zhang, Z. Gao, J. Zhang, P. Ge, F. Gao, J. Wang, F. Gao, Snapshot time-reversed ultrasonically encoded optical focusing guided by time-reversed photoacoustic wave, Photoacoustics 26 (2022), 100352, https://doi.org/10.1016/J.PACS.2022.100352.
[7] K.P. Kubelick, S.Y. Emelianov, In vivo photoacoustic guidance of stem cell injection and delivery for regenerative spinal cord therapies, Neurophotonics 7 (issue 3) (2020). https://doi.org/10.1117/1.NPH.7.3.030501.
[8] H.W. Baac, J.G. Ok, A. Maxwell, K.T. Lee, Y.C. Chen, A.J. Hart, Z. Xu, E. Yoon, L. J. Guo, Carbon-nanotube optoacoustic lens for focused ultrasound generation and high-precision targeted therapy, Sci. Rep. 2 (2012), https://doi.org/10.1038/srep00989.
[9] L. Shi, Y. Jiang, Y. Zhang, L. Lan, Y. Huang, J.X. Cheng, C. Yang, A fiber optoacoustic emitter with controlled ultrasound frequency for cell membrane sonoporation at submillimeter spatial resolution, Photoacoustics 20 (2020), https://doi.org/10.1016/j.pacs.2020.100208.
[10] T. Lee, H.W. Baac, Q. Li, L.J. Guo, Efficient photoacoustic conversion in optical nanomaterials and composites, Adv. Opt. Mater. 6 (2018), https://doi.org/10.1002/adom.201800491.
[11] B.Y. Hsieh, J. Kim, J. Zhu, S. Li, X. Zhang, X. Jiang, A laser ultrasound transducer using carbon nanofibers–polydimethylsiloxane composite thin film, Appl. Phys. Lett. 106 (2015), 021902, https://doi.org/10.1063/1.4905659.
[12] W.Y. Chang, W. Huang, J. Kim, S. Li, X. Jiang, Candle soot nanoparticles-polydimethylsiloxane composites for laser ultrasound transducers, Appl. Phys. Lett. 107 (2015), https://doi.org/10.1063/1.4934587.
[13] X. Du, J. Li, G. Niu, J.H. Yuan, K.H. Xue, M. Xia, W. Pan, X. Yang, B. Zhu, J. Tang, Lead halide perovskite for efficient optoacoustic conversion and application toward high-resolution ultrasound imaging, Nat. Commun. 12 (2021) 1–9, https://doi.org/10.1038/s41467-021-23788-4.
[14] Y. Hou, J.S. Kim, S. Ashkenazi, M. O'Donnell, L.J. Guo, Optical generation of high frequency ultrasound using two-dimensional gold nanostructure, Appl. Phys. Lett. 89 (2006), 093901, https://doi.org/10.1063/1.2344929.
[15] Z. Chen, Y. Wu, Y. Yang, J. Li, B. Xie, X. Li, S. Lei, J. Ou-Yang, X. Yang, Q. Zhou, B. Zhu, Multilayered carbon nanotube yarn based optoacoustic transducer with high energy conversion efficiency for ultrasound application, Nano Energy 46 (2018) 314–321, https://doi.org/10.1016/j.nanoen.2018.02.006.
[16] T. Buma, M. Spisar, M. O'Donnell, High-frequency ultrasound array element using thermoelastic expansion in an elastomeric film, Appl. Phys. Lett. 79 (2001) 548, https://doi.org/10.1063/1.1388027.
[17] J. Di, J. Kim, Q. Hu, X. Jiang, Z. Gu, Spatiotemporal drug delivery using laser-generated-focused ultrasound system, J. Control. Release 220 (2015) 592–599, https://doi.org/10.1016/j.jconrel.2015.08.033.
[18] M.R. Azani, A. Hassanpour, V. Carcelén, C. Gibaja, D. Granados, R. Mas-Ballesté, F. Zamora, Highly concentrated and stable few-layers graphene suspensions in pure and volatile organic solvents, Appl. Mater. Today 2 (2016) 17–23, https://doi.org/10.1016/J.APMT.2015.12.002.
[19] D.W. Johnson, B.P. Dobson, K.S. Coleman, A manufacturing perspective on graphene dispersions, Curr. Opin. Colloid Interface Sci. 20 (2015) 367–382, https://doi.org/10.1016/J.COCIS.2015.11.004.
[20] A.D. Silva, C.A. Henriques, D. v Malva, M.J.F. Calvete, M.M. Pereira, C. Serpa, L. G. Arnaut, Photoacoustic generation of intense and broadband ultrasound pulses with functionalized carbon nanotubes, Nanoscale 12 (2020) 20831–20839, https://doi.org/10.1039/D0NR04986G.
[21] A. Castellanos-Gomez, M. Buscema, R. Molenaar, V. Singh, L. Janssen, H.S.J. van der Zant, G.A. Steele, Deterministic transfer of two-dimensional materials by all-dry viscoelastic stamping, 2d Mater. 1 (2014), 011002, https://doi.org/10.1088/2053-1583/1/1/011002.
[22] P. Avouris, Graphene: electronic and photonic properties and devices, Nano Lett. 10 (2010) 4285–4294, https://doi.org/10.1021/nl102824h.
[23] F. Giorgianni, C. Vicario, M. Shalaby, L.D. Tenuzzo, A. Marcelli, T. Zhang, K. Zhao, Y. Chen, C. Hauri, S. Lupi, High-efficiency and low distortion photoacoustic effect in 3D graphene sponge, Adv. Funct. Mater. 28 (2018), https://doi.org/10.1002/adfm.201702652.
[24] D. Sun, Z.K. Wu, C. Divin, X. Li, C. Berger, W.A. de Heer, P.N. First, T.B. Norris, Ultrafast relaxation of excited dirac fermions in epitaxial graphene using optical differential transmission spectroscopy, Phys. Rev. Lett. 101 (2008), 157402, https://doi.org/10.1103/PhysRevLett.101.157402.
[25] T.V. Alencar, M.G. Silva, L.M. Malard, A.M. de Paula, Defect-induced supercollision cooling of photoexcited carriers in graphene, Nano Lett. 14 (2014) 5621–5624, https://doi.org/10.1021/nl502163d.
[26] A.L. McKenzie, Physics of thermal processes in laser-tissue interaction, Phys. Med. Biol. 35 (1990) 1175–1209, https://doi.org/10.1088/0031-9155/35/9/001.
[27] H.W. Baac, J.G. Ok, T. Lee, L. Jay Guo, Nano-structural characteristics of carbon nanotube-polymer composite films for high-amplitude optoacoustic generation, Nanoscale 7 (2015) 14460–14468, https://doi.org/10.1039/c5nr03769g.
[28] M. Xu, L. v Wang, Photoacoustic imaging in biomedicine, Rev. Sci. Instrum. 77 (2006), https://doi.org/10.1063/1.2195024.
[29] Z. Tao, H. Wang, X. Li, Z. Liu, Q. Guo, Expanded graphite/polydimethylsiloxane composites with high thermal conductivity, J. Appl. Polym. Sci. 134 (2017), https://doi.org/10.1002/APP.44843.
[30] N.S. Gupta, K.S. Lee, A. Labouriau, Tuning thermal and mechanical properties of polydimethylsiloxane with carbon fibers, Polymers 13 (2021), https://doi.org/10.3390/polym13071141.
[31] Y.F. Zhang, Y.J. Ren, H.C. Guo, S. lin Bai, Enhanced thermal properties of PDMS composites containing vertically aligned graphene tubes, Appl. Therm. Eng. 150 (2019) 840–848, https://doi.org/10.1016/j.applthermaleng.2019.01.029.
[32] A. Müller, M.C. Wapler, U. Wallrabe, A quick and accurate method to determine the Poisson's ratio and the coefficient of thermal expansion of PDMS, Soft Matter 15 (2019) 779–784, https://doi.org/10.1039/c8sm02105h.
[33] Y.H. Zhao, Z.K. Wu, S.L. Bai, Study on thermal properties of graphene foam/graphene sheets filled polymer composites, Compos. Part A Appl. Sci. Manuf. 72 (2015) 200–206, https://doi.org/10.1016/j.compositesa.2015.02.011.
[34] R. Gulotty, M. Castellino, P. Jagdale, A. Tagliaferro, A.A. Balandin, Effects of functionalization on thermal properties of single-wall and multi-wall carbon nanotube-polymer nanocomposites, ACS Nano 7 (2013) 5114–5121, https://doi.org/10.1021/nn400726g.
[35] J.D. Renteria, D.L. Nika, A.A. Balandin, Graphene thermal properties: applications in thermal management and energy storage, Appl. Sci. 4 (2014) 525–547, https://doi.org/10.3390/APP4040525.
[36] B.Y. Hsieh, J. Kim, J. Zhu, S. Li, X. Zhang, X. Jiang, A laser ultrasound transducer using carbon nanofibers–polydimethylsiloxane composite thin film, Appl. Phys. Lett. 106 (2015), 021902, https://doi.org/10.1063/1.4905659.

[37] H. Won Baac, J.G. Ok, H.J. Park, T. Ling, S.L. Chen, A.J. Hart, L.J. Guo, Carbon nanotube composite optoacoustic transmitters for strong and high frequency ultrasound generation, Appl. Phys. Lett. 97 (2010), 234104, https://doi.org/10.1063/1.3522833.
[38] R.J. Colchester, C.A. Mosse, D.S. Bhachu, J.C. Bear, C.J. Carmalt, I.P. Parkin, B. E. Treeby, I. Papakonstantinou, A.E. Desjardins, Laser-generated ultrasound with optical fibres using functionalised carbon nanotube composite coatings, Appl. Phys. Lett. 104 (2014), 173502, https://doi.org/10.1063/1.4873678.
[39] S. Noimark, R.J. Colchester, B.J. Blackburn, E.Z. Zhang, E.J. Alles, S. Ourselin, P. C. Beard, I. Papakonstantinou, I.P. Parkin, A.E. Desjardins, Carbon-nanotube–PDMS composite coatings on optical fibers for all-optical ultrasound imaging, Adv. Funct. Mater. 26 (2016) 8390–8396, https://doi.org/10.1002/ADFM.201601337.
[40] T. Lee, L.J. Guo, Highly efficient photoacoustic conversion by facilitated heat transfer in ultrathin metal film sandwiched by polymer layers, Adv. Opt. Mater. 5 (2017), https://doi.org/10.1002/adom.201600421.
[41] T. Lee, J.G. Ok, L.J. Guo, H.W. Baac, Low f-number photoacoustic lens for tight ultrasonic focusing and free-field micro-cavitation in water, Appl. Phys. Lett. 108 (2016), https://doi.org/10.1063/1.4943369.
[42] E. Herbert, S. Balibar, F. Caupin, Cavitation pressure in water, Phys. Rev. E Stat. Nonlin Soft Matter Phys. 74 (2006) 1–22, https://doi.org/10.1103/PhysRevE.74.041603.
[43] C.E. Brennen, Cavitation and bubble dynamics, Cavitation and Bubble Dynamics. 2013, 1–249. https://doi.org/10.1017/CBO9781107338760.
[44] M.A. Margulis, Sonoluminescence and sonochemical reactions in cavitation fields. A review, Ultrasonics 23 (1985) 157–169, https://doi.org/10.1016/0041-624X(85)90024-1.
[45] B.T. Muc, D. Vella, N. Lukač, M. Kos, M. Jezeršek, Generation of a focused pressure wave and localized cavitation clouds using a metal-semiconductor Ti/black-TiOx optoacoustic lens, Results Phys. 20 (2021), 103721, https://doi.org/10.1016/J.RINP.2020.103721.
[46] X.-X. Liang, N. Linz, S. Freidank, G. Paltauf, A. Vogel, Comprehensive analysis of spherical bubble oscillations and shock wave emission in laser-induced cavitation, J. Fluid Mech. 940 (2022) A5, https://doi.org/10.1017/JFM.2022.202.
[47] R.E. Apfel, C.K. Holland, Gauging the likelihood of cavitation from short-pulse, low-duty cycle diagnostic ultrasound, Ultrasound Med. Biol. 17 (1991) 179–185, https://doi.org/10.1016/0301-5629(91)90125-G.
[48] A.D. Maxwell, T.Y. Wang, L. Yuan, A.P. Duryea, Z. Xu, C.A. Cain, A tissue phantom for visualization and measurement of ultrasound-induced cavitation damage, Ultrasound Med. Biol. 36 (2010) 2132–2143, https://doi.org/10.1016/j.ultrasmedbio.2010.08.023.
[49] J. Laloš, P. Gregorčič, M. Jezeršek, Observation of laser-induced elastic waves in agar skin phantoms using a high-speed camera and a laser-beam-deflection probe, Biomed. Opt. Express 9 (2018) 1893, https://doi.org/10.1364/boe.9.001893.
[50] H.-C. Hsu, K.A. Wear, T. Joshua Pfefer, W.C. Vogt, Tissue-mimicking phantoms for performance evaluation of photoacoustic microscopy systems, Biomed. Opt. Express 13 (2022) 1357, https://doi.org/10.1364/boe.445702.
[51] M.O. Culjat, D. Goldenberg, P. Tewari, R.S. Singh, A review of tissue substitutes for ultrasound imaging, Ultrasound Med. Biol. 36 (2010) 861–873, https://doi.org/10.1016/j.ultrasmedbio.2010.02.012.
[52] H. Feiszthuber, S. Bhatnagar, M. Gyöngy, C.C. Coussios, Cavitation-enhanced delivery of insulin in agar and porcine models of human skin, Phys. Med. Biol. 60 (2015) 2421–2434, https://doi.org/10.1088/0031-9155/60/6/2421.
[53] A.D. Maxwell, T.Y. Wang, L. Yuan, A.P. Duryea, Z. Xu, C.A. Cain, A tissue phantom for visualization and measurement of ultrasound-induced cavitation damage, Ultrasound Med. Biol. 36 (2010) 2132–2143, https://doi.org/10.1016/J.ULTRASMEDBIO.2010.08.023.
[54] T. Drakos, A. Antoniou, N. Evripidou, T. Alecou, M. Giannakou, G. Menikou, G. Constantinides, C. Damianou, Ultrasonic attenuation of an agar, silicon dioxide, and evaporated milk gel phantom, J. Med. Ultrasound 29 (2021) 239–249, https://doi.org/10.4103/JMU.JMU_145_20.
[55] K.B. Bader, M.J. Crowe, J.L. Raymond, C.K. Holland, Effect of frequency-dependent attenuation on predicted histotripsy waveforms in tissue-mimicking phantoms, Ultrasound Med. Biol. 42 (2016) 1701–1705, https://doi.org/10.1016/j.ultrasmedbio.2016.02.010.
[56] C. Guittet, F. Ossant, J.P. Remenieras, L. Pourcelot, M. Berson, High-frequency estimation of the ultrasonic attenuation coefficient slope obtained in human skin: simulation and in vivo results, Ultrasound Med. Biol. 25 (1999) 421–429, https://doi.org/10.1016/S0301-5629(98)00176-8.
[57] B.I. Raju, M.A. Srinivasan, High-frequency ultrasonic attenuation and backscatter coefficients of in vivo normal human dermis and subcutaneous fat, Ultrasound Med. Biol. 27 (2001) 1543–1556, https://doi.org/10.1016/S0301-5629(01)00456-2.
[58] D. Bommannan, G.K. Menon, H. Okuyama, P.M. Elias, R.H. Guy, Sonophoresis. II. Examination of the mechanism(s) of ultrasound-enhanced transdermal drug delivery, Pharm. Res. 9 (1992) 1043–1047, https://doi.org/10.1023/A:1015806528336.
[59] S. Mitragotri, D. Blankschtein, R. Langer, Ultrasound-mediated transdermal protein delivery, Science 269 (1995) (1979) 850–853, https://doi.org/10.1126/SCIENCE.7638603.
[60] D.A. Pereira, A.D. Silva, P.A.T. Martins, A.P. Piedade, D. Martynowych, D. Veysset, M.J. Moreno, C. Serpa, K.A. Nelson, L.G. Arnaut, Imaging of photoacoustic-mediated permeabilization of giant unilamellar vesicles (GUVs), Sci. Rep. 11 (2021) 1–12, https://doi.org/10.1038/s41598-021-82140-4.
[61] B.E. Polat, D. Hart, R. Langer, D. Blankschtein, Ultrasound-mediated transdermal drug delivery: mechanisms, scope, and emerging trends, J. Control. Release 152 (2011) 330–348, https://doi.org/10.1016/j.jconrel.2011.01.006.
[62] E. Vranić, Sonophoresis-mechanisms and application, Bosn. J. Basic Med. Sci. 4 (2004) 25–32, https://doi.org/10.17305/BJBMS.2004.3410.

Dr. Daniele Vella studied at the School of Engineering at the University of Pisa, Italy. He joined the Department of Complex Matter (Jozef Stefan Institute, Ljubljana, Slovenia) as a Ph.D. student in Nanosciences and Nanotechnologies in 2013. His research activity involved the photo-physics of low-dimensional semiconductors and particularly 2D materials. After obtaining his Ph.D. in 2016, he continued his work at the National University of Singapore and the Center for Advanced 2D Materials. During his post-doc, he designed nanodevices and experiments to study the photoresponsivity and the electro-optic effects in van der Waals heterostructures made of transition metal dichalcogenides. He came back to Ljubljana in 2019 to join the Faculty of Mechanical Engineering as a research staff. His research activity is dedicated to develop photoacoustic nanomaterials and devices, study the photoacoustic response with short laser pulses, and apply them in medical science.

Dr. Vasyl Shvalya graduated from the Department of Semiconductors and Dielectrics at the Uzhhorod National University (Uzhhorod, Ukraine) in 2012. In 2017 he defended his Ph.D. thesis "Influence of isovalent dopants on critical behavior and dynamic thermal properties of Sn(Pb)2P2S(Se)6 ferroelectric crystals" and obtained a double doctoral degree in material science from Uzhhorod National University and the University of the Basque Country (Bilbao, Spain). Since 2018 he works as a researcher at the Jozef Stefan Institute, Department of Gaseous Electronic (Ljubljana, Slovenia). His field of expertise is mostly related to spectroscopic investigations of organic and inorganic materials using Raman, surface-enhanced Raman and infrared absorption, UV-vis, and X-ray photoelectron spectroscopic techniques. He is also interested in plasma/thermal synthesis, and modification of nanomaterials to improve analytical sensing devices in biochemical applications and life sciences.

Dr. Matija Jezeršek is associate professor and head of the Laboratory of Laser Techniques at the Faculty of Mechanical Engineering, University of Ljubljana. His research areas include laser materials processing, laser microstructuring, and inline optical monitoring systems for industrial and medical laser applications. He has published over 70 papers, filed 9 patents, and received several national awards for his research achievements.